



# Explaining the Multiwavelength Emission of Hard-TeV BL Lac Objects Using a Truncated Conical Jet Model

Maichang Lei<sup>1</sup>, Yuan Zheng<sup>1</sup>, Jianfu Zhang<sup>2</sup>, and Jiancheng Wang<sup>3</sup>

<sup>1</sup> College of Physics and Engineering Technology, Xingyi Normal University for Nationalities, Xingyi 562400, China; [maichanglei83@163.com](mailto:maichanglei83@163.com)

<sup>2</sup> Department of Physics, Xiangtan University, Xiangtan 411105, China

<sup>3</sup> Yunnan Observatories, Chinese Academy of Sciences, Kunming 650216, China

Received 2021 December 24; revised 2022 January 21; accepted 2022 January 27; published 2022 March 17

## Abstract

Hard-TeV BL Lac objects are newly identified populations of active galactic nuclei with the emitted  $\gamma$ -ray photons well above TeV energies. In this paper, we explain the multiwavelength emission of six Hard-TeV BL Lac objects by using a truncated conical emission region of the jet, where the electron distribution is obtained by numerically solving the evolution equation along the jet self-consistently. For comparison, we also apply the model to Mrk 421 and Mrk 501, which are the potential candidates for the hard TeV emissions. We demonstrate that the model can satisfactorily reproduce the spectral energy distributions of eight sources, particularly of six Hard-TeV sources, where no extreme minimum Lorentz factor of the electron population is required. In contrast with Mrk 421 and Mrk 501, six Hard-TeV sources have rather low magnetization in emitting regions and high cutoff energies of the electron distributions.

*Key words:* galaxies: active – (galaxies:) BL Lacertae objects: general – radiation mechanisms: non-thermal

## 1. Introduction

Blazars are jetted active galactic nuclei (AGNs) with bipolar relativistic plasma jet aligned closely with the line of sight (Urry & Padovani 1995; Padovani 2016). The nonthermal electromagnetic emission, covering a wider range from radio up to very high energy (VHE;  $E_\gamma \gtrsim 100$  GeV)  $\gamma$ -rays, is generally attributed to the jet and strongly enhanced by Doppler boosting. The multifrequency emissions are highly variable, on timescales of order of minutes to years (Abdo et al. 2010b). Blazars are subdivided, according to the broad emission line criterion (equivalent width  $>$  or  $< 5$  Å), into flat spectrum radio quasars (FSRQs) and BL Lacertae objects (BL Lacs) (Stickel et al. 1991; Stocke et al. 1991; Ghisellini et al. 2009). Based on the synchrotron peak,  $\nu_p^s$ , BL Lacs are further classified as low-peaked BL Lacs (LBL,  $\nu_p^s < 10^{14}$  Hz), intermediate-peaked BL Lacs (IBL,  $10^{14} \leq \nu_p^s \leq 10^{15}$  Hz) as well as high-peaked BL Lacs (HBL,  $\nu_p^s > 10^{15}$  Hz) (Abdo et al. 2010a). In contrast, BL Lacs commonly lack luminous external radiation fields, the accelerating electrons will suffer inefficient cooling and can be accelerated to higher energies within their jet. Accordingly, the peak energy of the radiated  $\gamma$ -ray photons will be up to several TeVs, this can be statistically depicted by “blazar sequence” (Fossati et al. 1998; Ghisellini et al. 1998, 2017).

Hard-TeV BL Lac objects (Hard-TeV BL Lacs) are an emerging class, and belong to extreme high-peaked BL Lacs (EHBLs) with the very high frequencies of their two emission peaks (Costamante et al. 2001; Şentürk et al. 2013;

Foffano et al. 2019; Biteau et al. 2020). These objects have an important implication to explore the extragalactic background light (EBL), the intergalactic magnetic fields and the exotic physics at extreme energies inaccessible with human-made devices, such as Lorentz invariance violation and axion-like particles (Biteau et al. 2020). A mini catalog of six Hard-TeV BL Lacs is presented by Costamante et al. (2018) (henceforth, Paper I), their characteristic Fermi-LAT spectra are well characterized by the hard spectral slope, typically,  $\Gamma_{\text{LAT}} \lesssim 1.6$ – $1.9$ , and their Compton peaks in spectral energy distribution (SED) are above 2–10 TeV. Comparatively, their synchrotron peaks are located at medium or hard X-ray bands. These characters lead a challenge to standard one-zone synchrotron self-Compton (SSC) model, where the Klein–Nishina (K-N) effect takes action to make the TeV spectrum steeper.

Various theoretical scenarios have been proposed to account for the origin of hard-TeV spectrum. They include the fine-tuned electron distributions with extremely hard Maxwellian form (Saugé & Henri 2004; Lefa et al. 2011), very high low-energy cutoff (Katarzyński et al. 2006; Tavecchio et al. 2009), large Doppler factor (Tavecchio et al. 2009), extreme model parameters (Tavecchio et al. 2010), and Compton upscattering of an external radiation field (Lefa et al. 2011) or internal  $\gamma$ - $\gamma$  absorption on a narrow-band radiation field (Aharonian et al. 2008). Moreover, the X-ray and TeV emissions are assumed to arise from distinct emitting regions (Böttcher et al. 2008). On the other hand, the hard-TeV spectra are also explored via invoking hadronic processes, e.g., as a secondary product of

cascades induced by ultra-high-energy protons (Essey & Kusenko 2010; Essey et al. 2011; Prosekin et al. 2012). For the archetypal Hard-TeV BL Lac 1ES 0229+200, its hard-TeV spectra are satisfactorily reproduced by intergalactic cascade scenario (Murase et al. 2012), or by the secondary radiations from p- $\gamma$  interaction (Cao & Wang 2014), but the latter needs highly super-Eddington jet power, which is about six orders of magnitude higher than the Eddington luminosity and could be problematic under the canonical accretion paradigm (Zdziarski & Bottcher 2015). Subsequently, Cerruti et al. (2015) applied the proton synchrotron and the p- $\gamma$ -induced cascades to interpret the hard-TeV spectra whereas avoiding the extreme parameters encountered in pure SSC models and super-Eddington crisis mentioned above. The TeV flares are also studied based on the hadronic and leptohadronic emission models (Murase et al. 2012; Cerruti et al. 2015; MAGIC Collaboration et al. 2019; Sahu et al. 2019). Recently, the broadband SEDs of several EHBs (including 1ES 0229+200) are modeled based on one-zone SSC, spine-layer and the proton synchrotron scenarios with substantially different parameters, especially for magnetization (Acciari et al. 2020).

The extremely high-energy photons from the Hard-TeV BL Lacs indicate that some efficient energization processes of particles in the relativistic jet must be at work. At present, three types of acceleration mechanism are preferred: the first-Fermi (shock), second-Fermi (stochastic) accelerations from the interactions of shock waves and of random field of Alfvén waves and magnetic reconnection usually adopted to explain the most rapid flares (Baring et al. 2017), which is notable incompatible with the modest variability shown by several Hard-TeV BL Lacs (Aliu et al. 2014; Cologna et al. 2015; Acciari et al. 2020). Among them, the shock and turbulence accelerations are widely invoked to accelerate particles to higher energies (Lewis et al. 2016, 2018; Baring et al. 2017). A hybrid acceleration process underwent by injected background particles, consisting of initial acceleration by turbulence followed by a second stage acceleration by shocks, could play an important role (Fan et al. 2010; Petrosian 2012; Kang 2015; Baring et al. 2017). The stochastic acceleration is also the promising candidate to produce the hard spectrum (Stawarz & Petrosian 2008; Asano et al. 2014). Most probably, the acceleration mechanisms operating during the flaring episodes could be their combination, with different dominated processes depending on the local conditions (Rieger et al. 2007). Under the dramatically low magnetization and the requirement on rather high energy electrons, the shocks and some preheating mechanisms, e.g., turbulent accelerations, could play a dominated role in the jet of the Hard-TeV BL Lacs (Zech & Lemoine 2021).

In this paper, we focus on the broadband SED modeling of six Hard-TeV BL Lacs presented in Paper I, with an emphasis on the origin of the hard-TeV spectrum. The outline of the paper is as follows. In Section 2, we outline the model

framework. Section 3 presents the model application. Results are discussed in Section 4 and the conclusions are given in Section 5. Throughout this paper, the following cosmological parameters are adopted:  $H_0 = 70 \text{ km s}^{-1} \text{ Mpc}^{-1}$ ,  $\Omega_M = 0.3$ ,  $\Omega_\Lambda = 0.7$ .

## 2. Model Description

In leptonic framework, while both conical and spherical configurations have been widely adopted as the emitting region to insight into the multiwavelength emission of blazars (Ghisellini et al. 1985; Moderski et al. 2003; Potter & Cotter 2012, 2013; Lei et al. 2018). Observationally, an axisymmetric jet flows, with a constant opening angle over much of the radical length, have been shown by Very Long Baseline Array (VLBA) images (Kovalev et al. 2007). Meanwhile, Sokolovsky et al. (2011) invoked this structure and well explained the frequency-dependent core shifts obtained by them. Therefore, this paper adopts the conical structure of magnetized jet to explore the nature of multi-wavelength emission from six Hard-TeV BL Lacs, where an assemble of isotropically non-thermal electrons are continually injected into a truncated conical region with radical length  $L'$  from the base, this truncated cone is called “emitting region” in the subsequent sections. It is emphasized that the primed quantities represent the ones measured in the comoving frame of the jet, whereas the quantities with subscript “obs” are measured in the observer’s frame. The emitting region is assumed to be filled with tangled magnetic field, the injected electrons are evolved following the evolution equation. Our model is the generalization of the one proposed by Potter & Cotter (2012) (henceforth, Paper II), this model mainly has two advantages, first, it can well reproduce the flat radio spectrum (Zheng & Yang 2016; Lei et al. 2018); second, compared with the models which involve to solve Fokker–Planck equation (Park & Petrosian 1996), it is quite appropriate for studying the BL Lacs in which only the simply cooling process needs to be considered, because it cannot deal with the complex cooling processes self-consistently. Thus, this only fits for Hard-TeV BL Lacs, a number of studies have shown that the  $\gamma$ -ray emitting region has rather weak magnetic field, the energy loss of the energetic electrons from inverse Compton cooling is very weak and can be ignored (Tavecchio et al. 2009; Kaufmann et al. 2011; Yan et al. 2012; Cohen et al. 2014; Costamante et al. 2018).

### 2.1. Diffusion Equation

The diffusion equation governing the evolution of the injected electron population along the jet is given by Paper II as

$$N'_e(\gamma', x' + dx') = N'_e(\gamma', x') - \frac{P'_{\text{tot}}(\gamma', x', dx')}{\gamma' m_e c^3}, \quad (1)$$

where  $N'_e(\gamma', x')$  represents the total distribution of electrons with energy  $\gamma' m_e c^2$  located at  $x'$ . In view of low magnetization

required for Hard-TeV BL Lacs, the evolution of electron population is dominated by synchrotron cooling, thus  $P'_{\text{tot}}$  roughly equals to  $P'_{\text{syn}}$ , the synchrotron power from electrons within a section of width  $dx'$ . In this paper, the radiating electrons are injected at the base and described by a single power-law energy distribution with an exponential cutoff  $\gamma'_{\text{cut}}$ :

$$N'_e(\gamma') = N_0 \gamma'^{-\alpha} e^{-(\gamma'/\gamma'_{\text{cut}})}, \quad (2)$$

the normalization  $N_0$  is related to the jet length and electron's energy in such a way:

$$A(\gamma', x') = N_0 \times \frac{N'_e(\gamma', x')}{N'_e(\gamma', x' = 0)}. \quad (3)$$

Subsequently, the synchrotron and SSC emissions can be calculated using the electron distribution given by

$$N'_e(\gamma', x') = A(\gamma', x') \gamma'^{-\alpha} \times e^{-(\gamma'/\gamma'_{\text{cut}})}. \quad (4)$$

## 2.2. Jet Energetics

The energetic electrons are injected into a narrower slab with width  $\Delta x'_{\text{inj}} = 1$  cm at the base of the emitting region, which moves along the jet with speed  $\beta_j c$ , accordingly, the jet's bulk Lorentz factor is  $\Gamma_j$ . The injected electron and magnetic energies are parameterized by  $E'_e$  and  $E'_B$ , which are related to the total energy in the lab frame as

$$\frac{E'_j}{\Gamma_j} = E'_e + E'_B, \quad (5)$$

we can therefore introduce equipartition fraction  $A_{\text{eq}} = E'_B/E'_e$ . Moreover, we assume that the magnetic field strength and the radius of the emitting region at the injected point are  $B'_0$  and  $R_0$ , respectively. Based on above assumptions, the injected energies can be further expressed as

$$\begin{aligned} E'_e &= m_e c^2 \int_{\gamma'_{\text{min}}}^{\gamma'_{\text{max}}} \gamma' N'_e(\gamma') d\gamma', \\ E'_B &= \pi R_0^2 \frac{B_0'^2}{8\pi}, \\ E'_e &= \frac{E_j^*}{\Gamma_j(1 + A_{\text{eq}})}, \\ E'_B &= \frac{A_{\text{eq}} E_j^*}{\Gamma_j(1 + A_{\text{eq}})}. \end{aligned} \quad (6)$$

Combining these equations,  $N_0$  and  $R_0$  can be calculated as follows:

$$\begin{aligned} N_0 &= \frac{E_j^* \mathcal{H}(\alpha, \gamma'_{\text{min}}, \gamma'_{\text{max}})}{\Gamma_j(1 + A_{\text{eq}})}, \\ R_0 &= \sqrt{\frac{8A_{\text{eq}} E_j^*}{\Gamma_j B_0'^2 (1 + A_{\text{eq}})}}, \end{aligned} \quad (7)$$

where the factor  $\mathcal{H}$  is determined merely by three quantities, i.e., the spectral index  $\alpha$ , the minimum  $\gamma'_{\text{min}}$  and the maximum  $\gamma'_{\text{max}}$  of the injected electron distribution. Moreover, we assume that each segment of the jet will conserve the magnetic energy, the magnetic field will decline as the function of radius of the jet, that is,

$$B'(x') = B'_0 \frac{R_0}{R(x')}. \quad (8)$$

We can approximately express the duration of the injected total energy into the emitting region as  $t'_{\text{inj}} = 1/(\Gamma_j \beta_j c)$ , in which the comoving length of  $\Delta x'_{\text{inj}} = 1$  cm has transformed into the lab frame following the simple Lorentz contraction, such that the injected jet power is given by  $P_j^* \approx E_j^*/t'_{\text{inj}} = E_j^* \Gamma_j \beta_j c$ .

## 2.3. Radiative Processes

The electrons are once injected into the emitting region and will diffuse along the jet, these electrons will inevitably produce emissions through synchrotron and SSC processes in the magnetic field. The synchrotron emissivity from electrons in a section of length  $dx'$  is given as

$$\begin{aligned} j'_{\text{syn}}(\epsilon', x') &= \frac{\sqrt{3} e^3 B'(x')}{h\pi R(x')^2} \int_{\gamma'_{\text{min}}}^{\gamma'_{\text{max}}} d\theta' d\gamma' N'_e(\gamma', x') \\ &\quad \times \mathcal{F}_{\text{syn}}(\epsilon'/\epsilon'_c) \sin \theta', \end{aligned} \quad (9)$$

where  $e$  is the electron charge,  $h$  is the Planck's constant,  $\theta'$  is the scattering angle of the velocity of electron with respect to the magnetic orientation,  $\mathcal{F}_{\text{syn}}(\epsilon'/\epsilon'_c) = \epsilon'/\epsilon'_c \int_{\epsilon'/\epsilon'_c}^{\infty} K_{5/3}(y) dy$  is the synchrotron scattering kernel,  $K_{5/3}$  is the modified Bessel function of order 5/3,  $\epsilon'_c$  is the characteristic dimensionless energy, given by

$$\epsilon'_c(\gamma', \theta', x') = \frac{3ehB'(x')\gamma'^2 \sin \theta'}{4\pi m_e^2 c^3}. \quad (10)$$

We note that Equation (9) need to be corrected by the factor  $(1 - e^{-k_{\epsilon'}(\epsilon', x')R(x')})$ , because of the synchrotron self-absorption, where  $k_{\epsilon'}$  is the opacity. It is noted that the path length of a photon with energy  $\epsilon'$  escaped from a segment of width  $dx'$  has approximately taken as  $R(x')$ , the radius of the jet, where the photon is produced. Combining this correction factor and Equation (9), the energy density of the synchrotron radiation can be given as

$$u'(\epsilon', x') \simeq \frac{R(x')}{c} j'_{\text{syn}}(\epsilon', x') [1 - e^{-k_{\epsilon'}(\epsilon', x')R(x')}]. \quad (11)$$

For a photon survived after undergoing a path length  $dx'$  will suffer from the absorption of the remaining part of the emitting region, which will incorporate another correction factor, thus the total synchrotron emissivity emitted by the whole truncated

cone is given by

$$J'_{\text{syn}}(\epsilon') = \sum_{x'} J'_{\text{syn}}(\epsilon', x') e^{-\tau_{\text{tot}}(\epsilon', x')} \quad (12)$$

where  $\tau_{\text{tot}}(\epsilon', x')$  is the opacity accounting for the absorption probability of a synchrotron photon moving from  $x'$  to  $L'$ .

We calculate the inverse Compton emission in which the effect of the cross section reduction in the K-N regime has been considered. So, the SSC emissivity is given by

$$J'_{\text{ssc}}(\epsilon'_s) = \frac{3}{4} c \sigma_{\text{T}} \epsilon'_s \sum_{x'} \int_0^{\infty} d\epsilon' \frac{u'(\epsilon', x')}{\epsilon'^2} \times \int_{\gamma'_{\text{min}}}^{\gamma'_{\text{max}}} d\gamma' \frac{N'_e(\gamma', x')}{\gamma'^2} \mathcal{F}_{\text{ssc}}(q, \Gamma_e) H(q; \frac{1}{4\gamma'^2}, 1), \quad (13)$$

where  $H$  is the Heaviside function,  $\mathcal{F}_{\text{ssc}}$  is the Compton scattering kernel for isotropic radiation fields of both photons and electrons, which has been given by Jones (1968), Blumenthal & Gould (1970), Finke et al. (2008), Dermer et al. (2009):

$$\mathcal{F}_{\text{ssc}}(q, \Gamma_e) = 2q \ln q + (1 + 2q)(1 - q) + \frac{1}{2} \frac{(\Gamma_e q)^2}{(1 + \Gamma_e q)} (1 - q), \quad (14)$$

with

$$q \equiv \frac{\epsilon'_s / \gamma'}{\Gamma_e (1 - \epsilon'_s / \gamma')}, \quad \Gamma_e \equiv 4\gamma' \epsilon'. \quad (15)$$

From Equations (12) and (13), the observed synchrotron and SSC fluxes are calculated according to

$$\epsilon F_{\epsilon}^{\text{Syn}} = \frac{\delta_{\text{D}}^4}{4\pi d_{\text{L}}^2} \epsilon' J'_{\text{syn}}(\epsilon'),$$

$$\epsilon_s F_{\epsilon_s}^{\text{SSC}} = \frac{\delta_{\text{D}}^4}{4\pi d_{\text{L}}^2} \epsilon'_s J'_{\text{syn}}(\epsilon'_s) e^{-\tau_{\text{EBL}}(\epsilon_s^{\text{obs}}, z)}, \quad (16)$$

where  $\delta_{\text{D}} = 1/[\Gamma_j(1 - \beta_j \cos(\theta_{\text{obs}}))]$  is the Doppler factor,  $\theta_{\text{obs}}$  is the viewing angle,  $d_{\text{L}}$  is the luminosity distance of the source with redshift  $z$ ,  $\tau_{\text{EBL}}$  is the optical depth responsible for the absorption of the VHE  $\gamma$ -ray photon by the EBL with the observed energy  $\epsilon_{\text{obs}}$  through electron–positron creation. In our model, the EBL model proposed by Franceschini et al. (2008) has been used. The energy of the observed photon is related to the one in the comoving frame by  $\epsilon_{\text{obs}} = \delta_{\text{D}} \epsilon' / (1 + z)$ .

#### 2.4. Numerical Implementation

For solving Equation (1) numerically, we need to discretize it as follows:

$$N'_e(\gamma'_i, x'_j) = N'_e(\gamma'_i, x'_{j-1}) - \frac{P'_{\text{tot}}(\gamma'_i, x'_{j-1})}{\gamma'_i m_e c^3}, \quad (17)$$

where  $\gamma'_i$ ,  $x'_j$  and  $x'_{j-1}$  are the values at grid points  $i$ th,  $j$ th and  $(j - 1)$ th, respectively. These grid values are given with equal

logarithmic resolution, i.e.,  $\delta\xi = [\log(\xi'_{\text{max}}) - \log(\xi'_{\text{min}})]/m$ , where  $\xi$  represents  $\gamma'$  or  $x'$ ,  $m$  is the meshpoint number.

Obviously, the initial electron distribution is once given, Equation (17) can be solved iteratively. To ensure the right-hand of Equation (17) has non-negative solution, a requirement has been imposed on the integral interval, such as  $dx' < c dt'_{\text{syn},c}$ , where  $t'_{\text{syn},c} \simeq \gamma'_{\text{cut}} m_e c^2 / P'_{\text{syn}}$  is the synchrotron cooling time for the injected electron population with cutoff energy,  $\gamma'_{\text{cut}}$ . The grid points can thus be swept over  $x'$  in an iterative way, i.e.,  $x'_i = x'_{i-1} + dx'$ .

Formally, the proposed model has 11 adjustable parameters, in which four parameters are used to describe the environment of the emitting region, i.e., the length  $L'$ , the magnetic field strength  $B'_0$  at the base, the bulk Lorentz factor  $\Gamma_j$  and the equipartition fraction  $A_{\text{eq}}$ ; the other four parameters,  $\alpha$ ,  $\gamma'_{\text{min}}$ ,  $\gamma'_{\text{max}}$ ,  $\gamma'_{\text{cut}}$ , are adopted to depict the electron distribution responsible for the multiwavelength emission; the two parameters,  $\theta_j^*$ ,  $\theta_{\text{obs}}$ , are the half-opening angle of the jet and the viewing angle. Moreover, we introduce an important quantity to represent the injected total energy, that is,  $E_j^*$ . However, these parameters can be further reduced by fixing some of them, specifically,  $L'$  is fixed at 1.0 pc,  $\gamma'_{\text{min}}$  and  $\gamma'_{\text{max}}$  are fixed at 1.0 and  $5.0 \times 10^7$ , whereas  $\theta_j^*$  and  $\theta_{\text{obs}}$  are respectively fixed at  $2^\circ 0$  and  $1^\circ 2$ , and the jet is thus aligned with the line of sight. Finally, the actual parameters are reduced to six:  $B'_0$ ,  $\Gamma_j$ ,  $A_{\text{eq}}$ ,  $\alpha$ ,  $\gamma'_{\text{cut}}$  and  $E_j^*$ . In the following, we perform the SED modeling for the sources by merely adjusting these six parameters.

### 3. Applications

In the following, the model is applied to six Hard-TeV BL Lacs presented in Paper I, where preliminary SED modelings have been performed and the results revealed that the rather low magnetic field, of the order of mG, could be possible. Observationally, this extreme subclass of blazar usually showed mild flux variations, with the flux variation of a factor of two to three, over years at TeV energies (Aliu et al. 2014; Cologne et al. 2015; Acciari et al. 2020). An exception is 1ES 1218+304, which presents a rapid flare over a few days (Acciari et al. 2010b). Even though these sources showed weak flux variation at  $\gamma$ -rays, but at other frequencies, because of the large statistical uncertainties, the notable flux variation cannot be ruled out, such as X-ray. Interestingly, Mrk 501, a prototypical high-peaked BL Lac object, also showed EHBL-like behaviors during its flaring episodes (Ghisellini 1999; Ahnen et al. 2018), this indicates that the HBLs could be the candidate to produce the hard-TeV emission under flaring states. However, in this paper, we apply the model to Mrk 421 and Mrk 501 when they were in low  $\gamma$ -ray state, instead, there remains some flux change at other frequencies, this will help us to compare the properties of two extreme subclasses of BL Lacs in roughly same state of activity, and provide an

explanation on why two HBLs cannot emit hard-TeV emission in non-flaring conditions, such a comparison will provide some clues on unveiling the origin of the Hard-TeV emission from the Hard-TeV BL Lacs. The SED data used for Mrk 421 and Mrk 501 are taken from 2008 August 5 to 2010 March 12 as well as 2009 March 15 to August 1, respectively (Abdo et al. 2011a, 2011b), where the quasi-simultaneous SED was reproduced using a one-zone leptonic SSC model and one-zone hadronic one. Under the former, the electron distribution is typically parameterized with two breaks, which indicates the complex acceleration and cooling processes of electrons would occur within the emitting region. In contrast, we attempt to reproduce the spectral shape by using electron distribution with only one break.

### 3.1. To Six Hard-TeV BL Lac Objects

First, the model is used to reproduce the broadband SED of six Hard-TeV BL Lacs, i.e., 1ES 0229+200, 1ES 0347–121, 1ES 0414+009, RGB J0710+591, 1ES 1101–232 and 1ES 1218+304. The multiwavelength data points are from Paper I, and are here presented in Figure 1, in which the red filled circles represent the quasi-contemporaneous data, the data points taking close to the same epoch of the VHE ones are shown as blue filled circles, the archival data are plotted in gray triangles. The VHE data of RGB J0710+591 and 1ES 1218+304 are taken by VERITAS telescopes, while the corresponding data are from HESS telescopes for other sources, these data sets have been corrected for EBL absorption using the model of Franceschini et al. (2008).

Figure 1 shows the resulting SED modeling to six Hard-TeV BL Lacs. Overall, the model can well reproduce the multi-frequency emission from radio to VHE  $\gamma$ -rays. An exception is 1ES 0414+009, its  $\gamma$ -ray emission cannot be well explained by our model, the dramatic incompatibility between flat Fermi-LAT spectrum and hard-TeV ones may originate from distinct SED emission component at different epochs, as stated in Paper I. Within this period, 1ES 0414+009 has likely changed its emitting state and with different  $\gamma$ -ray SED properties, making the Compton peak shift to higher frequency. On the other hand, it is worth mentioning that the data points are at optical, where the predominant emission is contributed by the host galaxy and not considered in our SED modeling, these data points only act as an upper limit to the reproduced spectrum. The model parameters are presented in Table 1, and the seven derived quantities are given in Table 2.

From Table 1, it is clear that the magnetic field strength  $B'_0$  at the base of the emitting region are of the order of magnitude of mG, which are roughly consistent with the ones adopted by Paper I. A larger value of  $B'_0$  is required for 1ES 0414+009, where  $B'_0$  takes 17 mG, which is about 18 times larger than that adopted in Paper I. The model requires an unusually low magnetic field to make the magnetic energy,  $U'_B$ , far below the

electron energy,  $U'_e$ , by two to three orders of magnitude. On the other hand, because of low magnetic energy, the electrons can be easily accelerated to higher energy under weak radiative cooling from synchrotron process. As shown in Figure 1, the good consistency of both flux and slope between the Fermi-LAT and the intrinsic VHE spectra suggest that the Compton peak would be located at the high-energy end or beyond, which is roughly related to the cutoff energy of electron distribution. Table 1 presents large value of  $\gamma'_{\text{cut}}$ , within the range of  $(1.0\text{--}8.8) \times 10^6$ , they are somewhat larger than the ones obtained by Paper I, where the maximum is  $1.5 \times 10^6$  for 1ES 0229+200. In our modeling, the larger value of  $8.8 \times 10^6$  is invoked for modeling the broadband SED of 1ES 0347–121, accordingly, this makes the Compton peak being at higher frequency. In comparison with 1ES 0347–121, the Compton peak of the other sources is nearly located at the tail of VERITAS or HESS observation. If this is true, the good energy coverage of the imaging atmospheric Cherenkov telescopes is vital to constrain on the high-energy peak of this unique subclass of blazar, and consequently to unveil the underlying acceleration processes.

A crucial parameter,  $\alpha$ , is closely related to the acceleration mechanisms of the particle, and the very hard spectral index is generally thought to be the typical property of the Hard-TeV BL Lacs at  $\gamma$ -rays. Our SED modeling requires  $\alpha$  to be within the range from 1.63 to 2.1, where four sources, 1ES 0229+200, 1ES 0347–121, RGB J0710+591 and 1ES 1218+304, have harder spectra, the corresponding  $\alpha$  are 1.63, 1.75, 1.7 and 1.8, respectively. In contrast, two sources, 1ES 0414+009 and 1ES 1218+304, have softer spectra with the same spectral index of 2.1. These values are basically consistent with  $n_1$  given in Paper I. In comparison with Paper I, 1ES 0229+200 and 1ES 1218+304 have obvious differences. For 1ES 0229+200, our obtained  $\alpha$  is 1.63 larger than their value of 1.4, while for 1ES 0229+200, the obtained value of 2.1 by us is obviously lower than their value of 2.85.

Once the broadband SEDs are well reproduced, the synchrotron and SSC peaks are shown in Table 3, where for each source the synchrotron and the SSC peaks have nearly the same flux level. Our SED modeling shows that five of the Hard-TeV BL Lacs have SSC peak, measured in the observer's frame, are well TeV energies, and the highest peak frequency of 1ES 0229+200 reaches 10.75 TeV. In contrast, 1ES 0414+009 has low SSC peak, which is located at 0.23 TeV. According to the Doppler transformation, we can obtain the comoving frequency of peak. From Table 3, we can see that the intrinsic SSC peaks of six Hard-TeV BL Lacs are lower than 1 TeV.

In Figure 2, we present the evolution of the electron population, under the well representation to the broadband SED in Figure 1, along the jet for six hard-TeV BL Lacs. In our code, 12 curves with the same logarithmic step are calculated and plotted, however, due to the weak cooling exists, only a

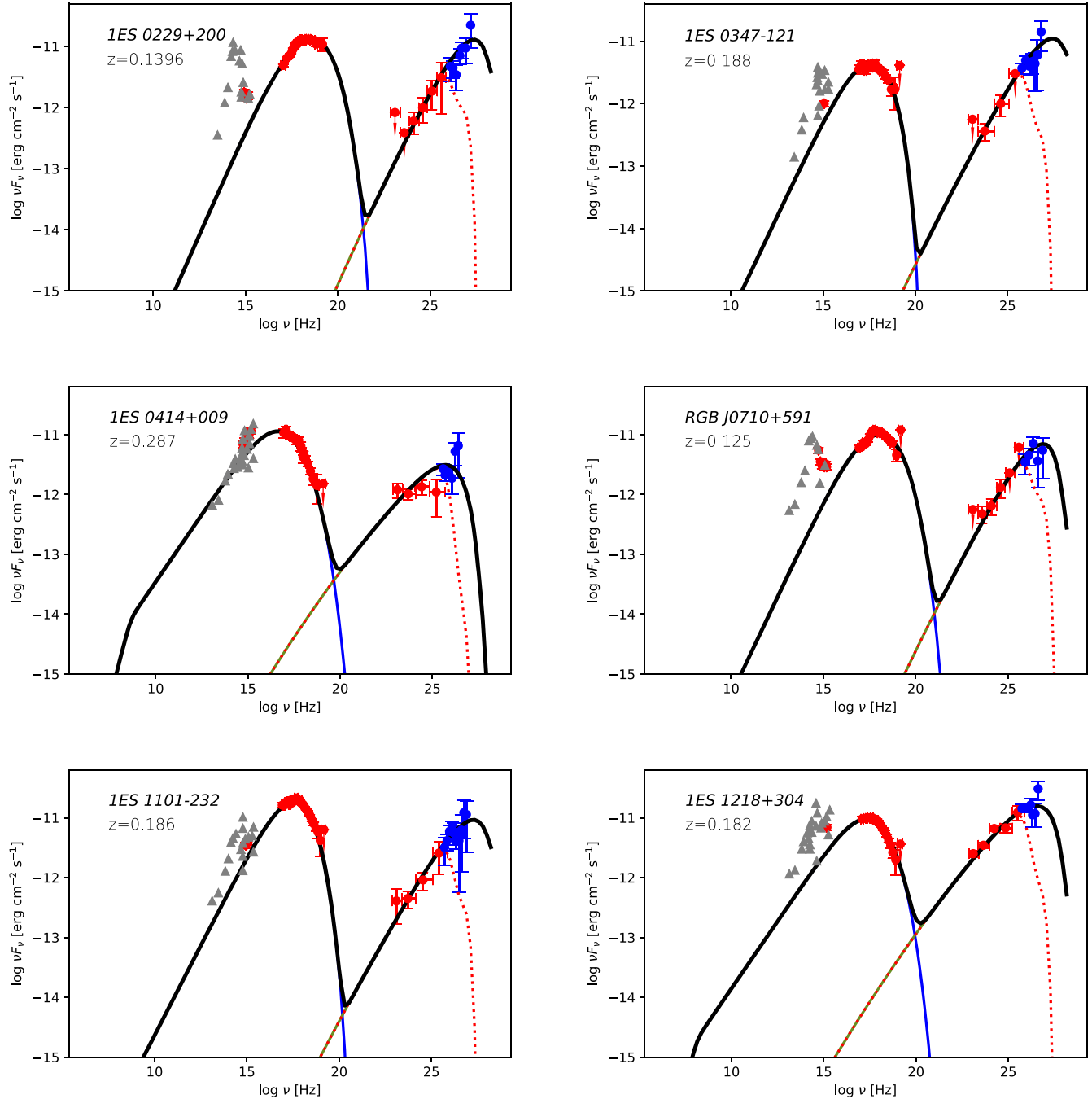


**Figure 1.** Broadband SED modelings to six Hard-TeV BL Lacs. The heavy black line indicates the superposed intrinsic emission from synchrotron and SSC processes, the blue solid line represents the synchrotron emission and the red dotted-line is the EBL-corrected SSC spectrum using the EBL model proposed by Franceschini et al. (2008).

few curves are shown. Because of distinct emitting conditions, the number of the curve is different for different sources. From right to left, a set of curves represent the electron distributions at the location from the base of the emitting region. It is clear that the spectral shape hardly keeps invariable for each location as long as the Lorentz factor of the electrons is below the

cutoff, while above the cutoff the curve will bend down, this can be contributed to the exponential cutoff itself, the synchrotron cooling or K-N effect, or their combination. As for the K-N effect, the decline of the scattering cross-section will largely decrease the collisions between high-energy electrons and photons to low the flux at the high-energy end.

**Table 1**  
Input Parameters for the Model

Source	$B'_0$ (mG)	$\Gamma_j$	$\alpha$	$\gamma'_{\text{cut}}$	$A_{\text{eq}}$	$E_j^*$ (erg s $^{-1}$ )	$\log \left[ \frac{M_{\text{BH}}}{M_\odot} \right]$
IES 0229+200	3.7	23	1.63	$6.7 \times 10^6$	$6.1 \times 10^{-3}$	$4.3 \times 10^{29}$	9.2 (a)
IES 0347–121	0.11	18	1.75	$8.8 \times 10^6$	$1.6 \times 10^{-4}$	$2.2 \times 10^{31}$	8.7 (b)
IES 0414+009	17	18	2.1	$9.7 \times 10^5$	$6.2 \times 10^{-2}$	$7.2 \times 10^{31}$	9.3 (c)
RGB J0710+591	8.2	16	1.7	$3.8 \times 10^6$	$2.6 \times 10^{-2}$	$4.9 \times 10^{29}$	8.3 (d)
IES 1101–232	0.17	19	1.8	$7.3 \times 10^6$	$5.7 \times 10^{-3}$	$3.6 \times 10^{31}$	9 (e)
IES 1218+304	2.1	16	2.1	$4.5 \times 10^6$	$2.2 \times 10^{-4}$	$2.8 \times 10^{32}$	8.6 (f)
Mrk 421	$1.0 \times 10^3$	33	1.81	$6.9 \times 10^4$	1.4	$6.2 \times 10^{29}$	8.3 (g)
Mrk 501	$4.4 \times 10^2$	21	2.2	$4.5 \times 10^5$	$1.1 \times 10^{-2}$	$5.1 \times 10^{30}$	9.2 (h)

**Note.**  $B'_0$ ,  $\Gamma_j$  are the magnetic field strength at the base and the bulk Lorentz factor of the jet, respectively.  $\alpha$  and  $\gamma'_{\text{cut}}$  are the spectral index and the cutoff energy for injected electron distribution, respectively.  $A_{\text{eq}}$  is the equipartition fraction between magnetic and electron's energy measured in the comoving frame,  $E_j^*$  is the injected energy. The last column represents the mass of the central BH, where the superscripts represent the corresponding references, such that: (a): Aharonian et al. (2007a), (b): Aharonian et al. (2007b), (c): Falomo et al. (2003), (d): Acciari et al. (2010a), (e): Aharonian et al. (2007c), (f): Acciari et al. (2009), (g): Albert et al. (2007a), (h): Albert et al. (2007b).

**Table 2**  
The Values of Several Derived Quantities

Source	$\delta_D$	$r'_{\text{em}}$ (pc)	$N_0$	$P_e^*$ (erg s $^{-1}$ )	$P_B^*$ (erg s $^{-1}$ )	$P_p^*$ (erg s $^{-1}$ )	$P_{\text{tot}}^*/L_{\text{Edd}}$
IES 0229+200	37.3	$5.5 \times 10^{-3}$	$1.4 \times 10^{34}$	$2.9 \times 10^{41}$	$1.8 \times 10^{39}$	$5.4 \times 10^{44}$	$2.7 \times 10^{-3}$
IES 0347–121	31.5	0.31	$1.1 \times 10^{36}$	$1.2 \times 10^{43}$	$1.9 \times 10^{39}$	$2.2 \times 10^{46}$	0.35
IES 0414+009	31.5	$6.9 \times 10^{-2}$	$4.6 \times 10^{36}$	$3.7 \times 10^{43}$	$2.3 \times 10^{42}$	$6.7 \times 10^{46}$	0.27
RGB J0710+591	28.8	$9.3 \times 10^{-3}$	$2.4 \times 10^{34}$	$2.3 \times 10^{41}$	$5.9 \times 10^{39}$	$4.2 \times 10^{44}$	$1.7 \times 10^{-2}$
IES 1101–232	32.8	1.4	$1.7 \times 10^{36}$	$2.0 \times 10^{43}$	$1.2 \times 10^{41}$	$3.7 \times 10^{46}$	0.3
IES 1218+304	28.8	$8.1 \times 10^{-2}$	$2.1 \times 10^{37}$	$1.3 \times 10^{44}$	$2.9 \times 10^{40}$	$2.5 \times 10^{47}$	4.9
Mrk 421	44.7	$1.4 \times 10^{-4}$	$7.2 \times 10^{33}$	$2.6 \times 10^{41}$	$3.6 \times 10^{41}$	$4.7 \times 10^{44}$	$1.9 \times 10^{-2}$
Mrk 501	35.2	$2.4 \times 10^{-4}$	$3.2 \times 10^{35}$	$3.2 \times 10^{42}$	$3.5 \times 10^{40}$	$5.8 \times 10^{45}$	$2.9 \times 10^{-2}$

**Note.**  $\delta_D$  is the Doppler factor,  $r'_{\text{em}}$  is the distance from the central BH,  $N_0$  is the normalization of the electron distribution. The subsequent three columns,  $P_e^*$ ,  $P_B^*$ ,  $P_p^*$ , are the jet power loaded by energetic electrons, magnetic field and the cold protons, respectively. The last column represents the ratio between the total jet power to the Eddington luminosity. For calculating the jet power, one cold proton per electron has been assumed.

**Table 3**  
Peaks and Peaking Fluxes for Synchrotron and SSC Humps

Source	$\nu'_{\text{s,p}}$ (Hz)	$\nu_{\text{obs}}^{\text{s,p}}$ (Hz)	$f_{\epsilon}^{\text{Syn,p}}$ (erg cm $^{-2}$ s $^{-1}$ )	$\nu'_{\text{ssc,p}}$ (Hz)	$\nu'_{\text{ssc,p}}$ (TeV)	$\nu_{\text{obs}}^{\text{ssc,p}}$ (Hz)	$\nu_{\text{obs}}^{\text{ssc,p}}$ (TeV)	$f_{\epsilon_s}^{\text{SSC,p}}$ (erg cm $^{-2}$ s $^{-1}$ )
IES 0229+200	$1.3 \times 10^{17}$	$4.1 \times 10^{18}$	$1.3 \times 10^{-11}$	$7.9 \times 10^{25}$	0.33	$2.6 \times 10^{27}$	10.75	$1.3 \times 10^{-11}$
IES 0347–121	$1.7 \times 10^{16}$	$4.4 \times 10^{17}$	$4.6 \times 10^{-12}$	$7.9 \times 10^{25}$	0.33	$2.1 \times 10^{27}$	8.71	$1.1 \times 10^{-11}$
IES 0414+009	$2.2 \times 10^{15}$	$5.4 \times 10^{16}$	$1.1 \times 10^{-11}$	$2.3 \times 10^{24}$	0.0095	$5.6 \times 10^{25}$	0.23	$3.1 \times 10^{-12}$
RGB J0710+591	$4.6 \times 10^{16}$	$1.2 \times 10^{18}$	$1.0 \times 10^{-11}$	$2.9 \times 10^{25}$	0.12	$7.4 \times 10^{26}$	3.05	$7.0 \times 10^{-12}$
IES 1101–232	$1.7 \times 10^{16}$	$4.6 \times 10^{17}$	$1.9 \times 10^{-11}$	$7.9 \times 10^{25}$	0.37	$2.2 \times 10^{27}$	9.08	$9.2 \times 10^{-12}$
IES 1218+304	$1.0 \times 10^{16}$	$2.4 \times 10^{17}$	$9.6 \times 10^{-12}$	$1.0 \times 10^{25}$	0.04	$2.5 \times 10^{26}$	1.05	$1.6 \times 10^{-11}$
Mrk 421	$6.0 \times 10^{15}$	$2.6 \times 10^{17}$	$2.6 \times 10^{-10}$	$5.0 \times 10^{23}$	$2.07 \times 10^{-3}$	$2.2 \times 10^{25}$	0.09	$1.0 \times 10^{-10}$
Mrk 501	$1.0 \times 10^{16}$	$3.4 \times 10^{17}$	$5.3 \times 10^{-11}$	$8.3 \times 10^{23}$	$3.43 \times 10^{-3}$	$2.8 \times 10^{25}$	0.12	$3.3 \times 10^{-11}$

**Note.** The quantities with superscript “'” are given in comoving frame, while all quantities with subscript or superscript “p” indicate these quantities are the peaking value.

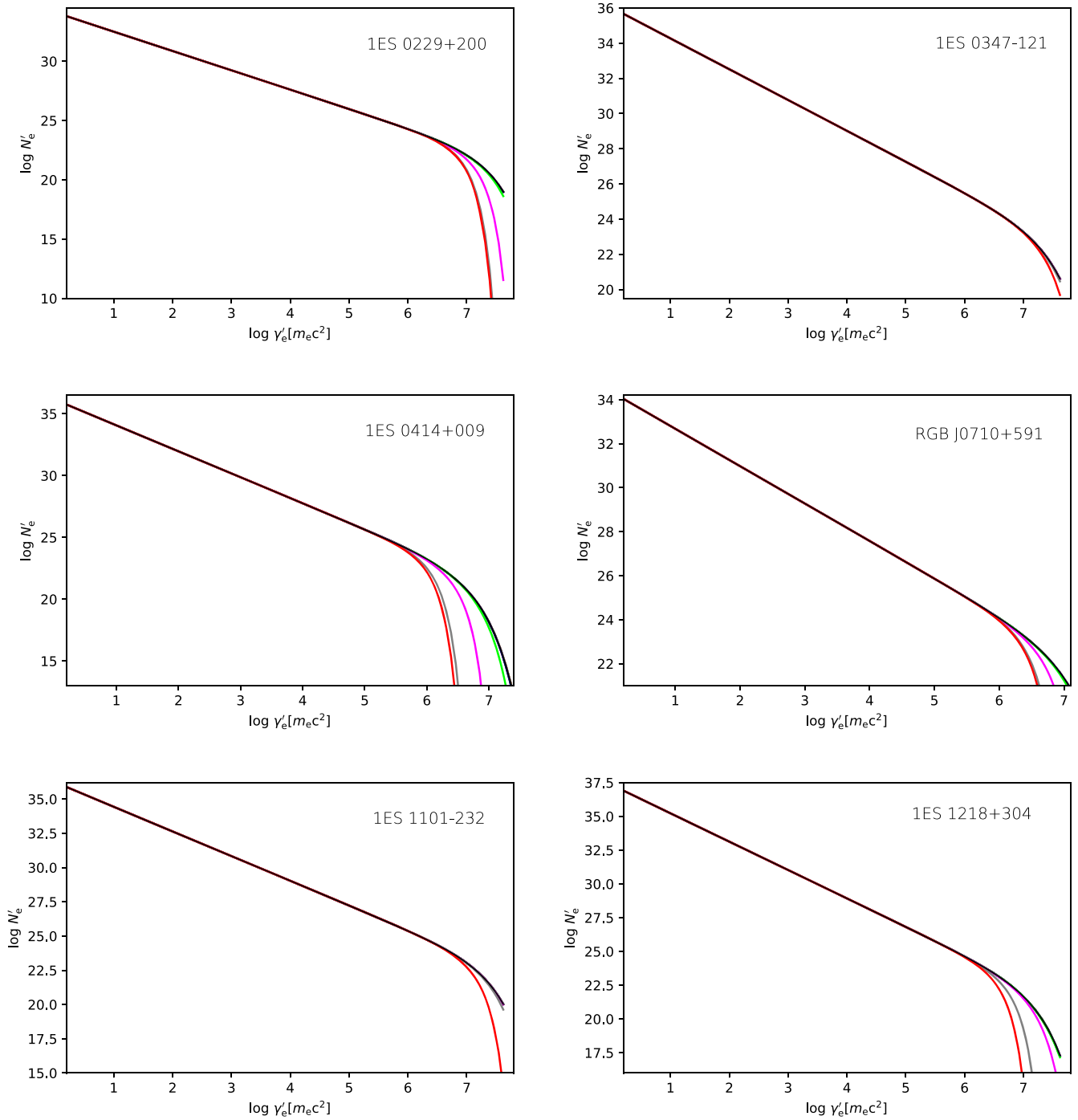


**Figure 2.** Electron number distribution vs. normalized energy  $\gamma'$  by  $m_e c^2$  for six Hard-TeV BL Lacs, which correspond to the SED modeling as shown in Figure 1. In each panel, the black line indicates the injected spectrum, whereas the remaining curves correspond to a series of grid points  $x'$  at further distance.

As shown in Figure 2, four sources show an excessive softening of the high-energy  $\gamma$ -ray spectrum, i.e., 1ES 0229+200, 1ES 0414+009, 1ES 1101-232 and 1ES 1218+304, the other two sources only show weak deviation from the

injected spectrum. Taking both  $B'$  and  $r'_{\text{em}}$  into account, the radiative cooling will play an important role in shaping VHE spectrum, where  $r'_{\text{em}}$  is the distance from the central black hole (BH) and is presented in Table 2. It is calculated via

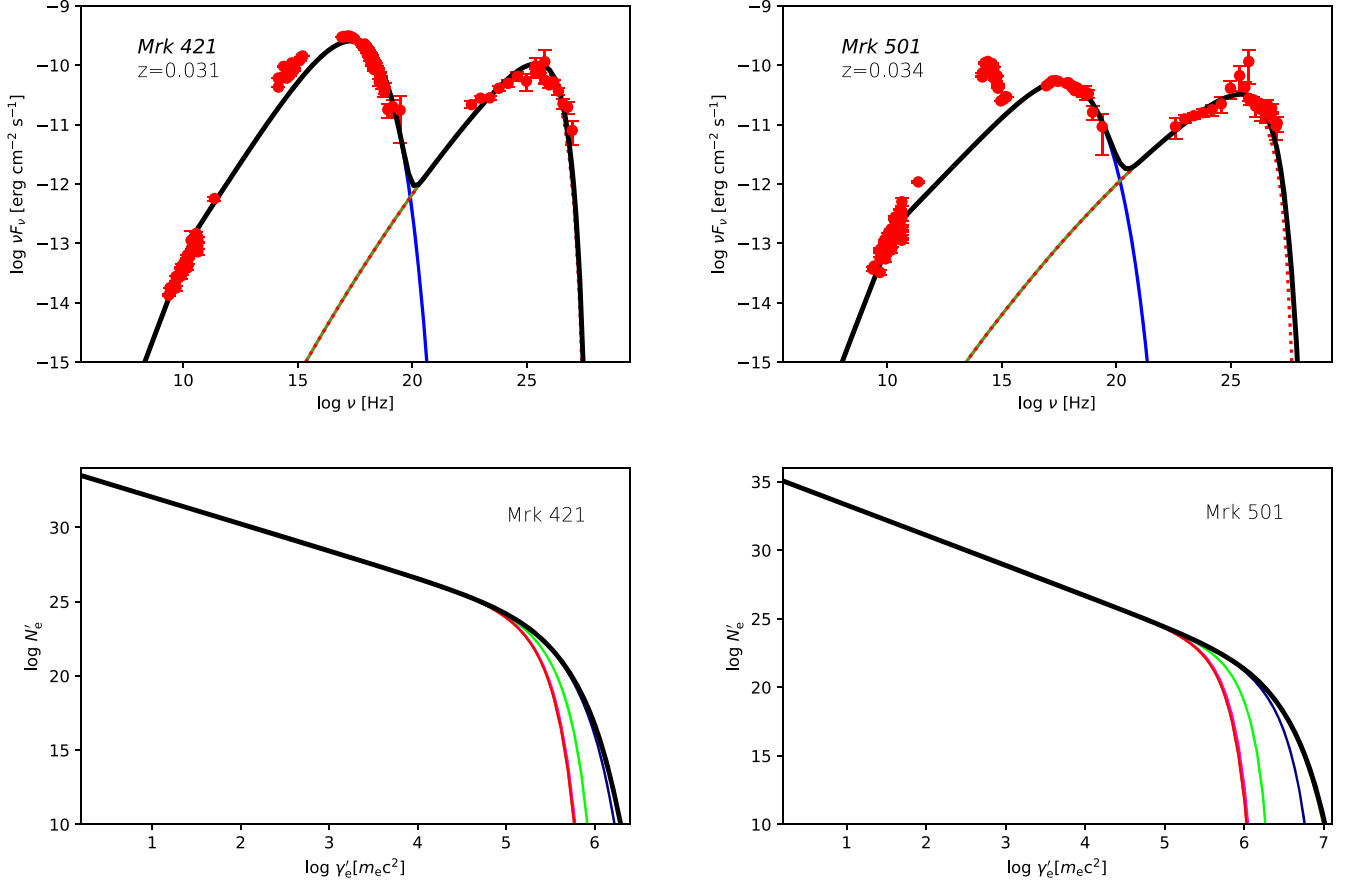


**Figure 3.** Broadband SED modeling for two typical HBLs, Mrk 421 (left column) and Mrk 501 (right column). In SED modelings, the heavy black line is the superposed spectrum from synchrotron and the SSC processes, the red dotted line is the EBL-corrected SSC emission using the EBL model proposed by Franceschini et al. (2008). For each source, the bottom panel corresponds to energy distribution of electrons at different  $x'$ , where the black line is the spectrum at the injected point. The remaining curves, from right to left, represent the spectra at further locations, respectively.

$r'_{\text{em}} = R_0 / \tan(\theta'_{\text{obs}})$ , where  $\theta'_{\text{obs}}$  is the viewing angle measured in the comoving frame, which is connected to  $\theta_{\text{obs}}$  by  $\tan(\theta'_{\text{obs}}) = \Gamma_j \tan(\theta_{\text{obs}})$ .

### 3.2. To HBLs Mrk 421 and Mrk 501

Figure 3 also shows the broadband SED modelings and the corresponding electron distributions, where Mrk 421 and Mrk 501 correspond to the left and right columns, respectively. The same as Figure 1, the optical data are not considered and in principle can be explained by invoking the contributions from the host galaxy. For Mrk 501, the optical data accumulated to a mini hump with distinct difference to the remainder of the synchrotron hump in terms of spectrum and flux level. However the optical data of Mrk 421 has the similar spectral slope connecting the radio and X-ray data, but has slightly higher flux level. In order to well model the data of both optical and X-ray, the model curve will unavoidably exceed the radio data, unless a large minimum Lorentz factor is adopted in electron distribution. Generally, the radio emission is thought

to be the superposition from the extended emission region, as shown in Lei et al. (2018). Therefore, the radio flux is commonly taken as an upper limit. In our SED modeling, the minimum Lorentz factor is fixed at 1.0, thus the model curve need to be below the optical data, this inversely implies that the optical data may be elevated by the emission from the host galaxy. As far as the spectral shape is considered, the spectrum of Mrk 421 is more steeper than that of Mrk 501 at low-energy frequencies before the synchrotron peak, this consequently requires a harder spectral index for Mrk 421 than for Mrk 501.

After these considerations, the broadband SED modelings are carried out. As mentioned above, a relatively hard spectral index is required for Mrk 421, but we cannot provide a well fitting to the beginning data of the SSC hump if a rather hard value is adopted. Inversely, if we adopt a relatively soft spectral index, the modeling curve will be above the radio data. To give a better fitting to all the observational data, we use soft spectral index and increase  $\Gamma_j$  to make the multifrequency spectrum shifting toward the higher frequency. The modeling curve will

pass through or low the radio data. On the other hand, we performed the SED modeling to Mrk 501 by taking a soft spectral index and a relatively low value of  $\Gamma_j$ . The resulting parameters are presented in Table 1, it is clear that both sources have different parameters, where Mrk 421 has the harder spectral index of 1.81, the higher magnetic field of 1.0 G at the base of the emitting region and the higher  $\Gamma_j$  of 33. Due to larger magnetic field, the equilibrium between matter and magnetic energies is achieved, e.g.,  $A_{\text{eq}}$  equals to 1.4. However, Mrk 501 has the soft spectral index of 2.2, the lower magnetic field of 0.44 G and the normal  $\Gamma_j$  of 21. Both sources have also significant difference in  $\gamma'_{\text{cut}}$ , corresponding to  $6.9 \times 10^4$  and  $4.5 \times 10^5$  for Mrk 421 and Mrk 501, respectively. Moreover, the peaks and fluxes of synchrotron and SSC humps are also presented in Table 3. Their synchrotron peaks have nearly the same value of frequency, but their SSC peaks are far below those of Hard-TeV BL Lacs.

In Figure 3, the bottom two panels show the evolution of emitting electrons with the distance from the central BH for Mrk 421 and Mrk 501. In comparison with six Hard-TeV BL Lacs, their electron populations have the same trend of evolution. Once the Lorentz factor of the electrons are over the cutoff energy  $\gamma'_{\text{cut}}$ , the electron distribution drops exponentially. Since the stronger magnetic field in the emitting region with respect to Hard-TeV BL Lacs, the high-energy electron spectrum shows significantly change above  $\gamma'_{\text{cut}}$ , in which the spectrum becomes steeper when the grid approaches to the end of the emitting region.

### 3.3. Jet Power

In leptonic scenario, the multiwavelength emission originates predominantly from the nonthermal electrons and positrons (shorted as electrons) within the tangled magnetic field, whereas the jet dynamics is dominated by the cold protons. In Table 2, we present the jet power loaded by electrons, magnetic field and the cold protons given by

$$\begin{aligned} P_e^* &= \Gamma_j^2 \beta_j c E_e', \\ P_B^* &= \Gamma_j^2 \beta_j c E_B', \\ P_p^* &= 1836 \Gamma_j^2 \beta_j c E_e'. \end{aligned} \quad (18)$$

The total jet power is given by  $P_j^* = P_e^* + P_B^* + P_p^*$ . It is emphasized that the jet power related to the protons is calculated assuming one cold proton per electron. In Table 2, we also show the ratio of the total jet power to the Eddington luminosity (Eddington ratio), the latter is given by  $L_{\text{Edd}} \simeq 1.26 \times 10^{38} M_{\text{BH}}/M_{\odot} \text{ erg s}^{-1}$ , where  $M_{\text{BH}}$  and  $M_{\odot}$  are the central BH mass and the solar mass, respectively. We can see from Table 2 that half of the eight sources has lower Eddington ratio, including 1ES 0229+200, RGB J0710+591 and two HBLs, at the order of  $10^{-3}$ . Other three hard-TeV BL Lacs, 1ES 0347–121, 1ES 0414+009 and 1ES 1101–232

have larger jet power nearly at the factor 0.3 of the Eddington luminosity. The maximum jet power appears in 1ES 1218+304 with the factor 4.9 of the Eddington luminosity.

## 4. Discussion

We reproduce the broadband SED of six Hard-TeV BL Lacs by using the power-law electron distributions with the exponential cutoff, where the injected electron distribution spans a broader range with the Lorentz factor,  $\gamma'$ , from 1.0 to  $5 \times 10^7$ . These electrons are injected and evolved following the diffusion equation. To fit well the hard-TeV data, we require relatively hard spectral index for 1ES 0229+200, 1ES 0347–121, RGB J0710+591 and 1ES 1101–232, while we adopt softer spectral index for 1ES 0414+009 and 1ES 1218+304. Their typical feature from the SED modeling is that the magnetic field strength at the injected point, as illustrated in Table 1, is at the order of mG, consistent with ones obtained by previous studies (i.e., Paper I). The weak magnetic field strength together with the short distance from the central BH could be problematic for powering the collimated outflow of the jet from sub-pc to kpc or even up to the spatial scale of the host galaxy, as illustrated by extensive radio observations. Actually, the collimation and acceleration take place up to hundreds of pc along the jet (Asada & Nakamura 2012; Hada et al. 2018), justified by the very long baseline interferometry (VLBI) by measuring kinematics of bright knots (Homan et al. 2009, 2015; Jorstad et al. 2017). Generally, a low magnetization favors the shock accelerations, however, from the point of view of internal shock scenarios (Spada et al. 2001), the particles will have low acceleration efficiency under the weak magnetization (Mimica & Aloy 2012; Rueda-Becerril et al. 2013, 2014). Therefore, such weak magnetic fields required for reproducing the hard-TeV spectra could be ‘‘abnormal’’ to relativistic jet, where the distribution of magnetic field is homogeneous transversely.

On the other hand, it is well known that magnetohydrodynamic (MHD) turbulence is believed to accelerate the electrons of relativistic jet in AGN. In realistic situation, MHD turbulence may be accompanied with shocks and magnetic reconnections occurring inside the magnetized jet. MHD simulations also suggest that the Fermi-I acceleration will give rise to higher levels of stochastic turbulence (Inoue et al. 2011), these turbulent processes will lead to the efficient acceleration of the injected particles. For inhomogeneous jet, the efficient re-acceleration processes will occur in the transition layer connecting the internal violently shocked spine and external stable sheath (Zech & Lemoine 2021). Considering MHD turbulent acceleration and synchrotron and SSC radiative losses, Uzdensky (2018) derived a relationship between rms Lorentz factor of the electrons and the optical depth as  $\gamma'_{\text{rms}} \propto \tau_{\text{T}}^{-1/2}$ . Thus, the higher the rms Lorentz factor is, the smaller the optical depth becomes. It is roughly

consistent with our results of SED modelings, in which the larger scale of the emitting region is used, the low jet power is required.

The model is also applied to two typical HBLs Mrk 421 and Mrk 501, we obtain distinct spectral characteristics with respect to Hard-TeV BL Lacs, corresponding to the stronger magnetic field and the lower value of  $\gamma'_{\text{cut}}$ , corresponding to 1.0 G and 0.44 G, respectively. We note that a detailed SED modeling based on the  $\chi^2$ -minimization technique using the simple one-zone syn+SSC leptonic model has been performed to investigate the radiation mechanisms and physical properties of the GeV–TeV BL Lacs, in which a slightly different values of parameters are given to low state (Zhang et al. 2012), however, the obtained values of  $B'_0$  remain higher than the ones of six Hard-TeV BL Lacs, such higher magnetic fields are also required to well interpret the multifrequency observations (Albert et al. 2007b; Acciari et al. 2011; Cao & Wang 2013; Yan et al. 2013; Zhang et al. 2013; Chen 2017; Zheng et al. 2018). Thus, Mrk 421 and Mrk 501 have different properties from the Hard-TeV BL Lacs, this is mostly independent of the special model adopted. In terms of the acceleration mechanism, an equipartition of the matter and the magnetic energy as well as a hard spectral index for Mrk 421 support that the magnetic reconnection could play an important role to energize the background particles, while the weak magnetic field and the softer spectral index for Mrk 501 prefer to suggest that the shock acceleration will take action in accelerating the particles.

It is well known that blazars commonly show the spine-sheath morphology in radio VLBI maps, i.e., a limb-brightening component was interpreted as a slower external flow surrounding a fast spine (Ghisellini et al. 2005), this morphology is also supported by the polarization VLBI observations (Zakamska et al. 2008), a clear spine-sheath polarization structure was first observed from quasar 1055+018 on parsec scales (Attridge et al. 1999), other strong observational supports for a spine-sheath structure to several TeV blazars were presented by Piner et al. (2009, 2010) and MacDonald et al. (2015). Moreover, Kravchenko et al. (2017) performed polarimetry analysis on 20 AGNs jets using VLBA, and the observed variety of polarized signatures can be explained by a model of spine-sheath jet structure. Thus, the spine-sheath structure has been the common morphology of the relativistic jet in blazars. Theoretically, the various models based on spine-sheath structure have been proposed to explain the origin of the orphan  $\gamma$ -ray flares, where a blob of plasma moving relativistically along the spine of the jet inverse-Compton scatter the diffuse synchrotron photons emanating from a shocked sheath plasma (MacDonald et al. 2015, 2017). (iii). The broadband SED of the Hard-TeV HBL 2WHSP J073326.7+515354 can be better represented by a two-zone spine-layer model than the standard one-zone leptonic scenario (MAGIC Collaboration et al. 2019). Such a structured jet is

also used to explore the origin of the high-energy neutrinos detected by IceCube (Tavecchio et al. 2014).

For spine-sheath structure, the higher magnetic field exists in the spine, while the magnetic field within the sheath is significantly weak, the speed of the internal spine flow is much larger than the external sheath flow. The high-energy electron populations originate presumably from the spine, where some efficient acceleration mechanisms will be at work, the high-energy electrons will be produced and reaccelerated continually along the spine. As the particle energy increases and the magnetic field declines, their Larmor radius becomes more larger. As a consequence, the high-energy electrons will go away from the spine, and naturally diffuse into the sheath. Hillas (1984) has shown that a particle with a larger Larmor radius will travel preferentially closer to the edge or sheath of the jet, where the apparent magnetic field strength may be much less than that of the spine. Due to lower synchrotron radiation field and weak magnetic field, these electrons will suffer from relatively low radiative loss. Also, the K-N turnover will also bring about inefficient energy losses at high-energy end. Maybe, at the interface between the spine and the sheath, the collisions of both shocks and surrounding matter induce outstanding turbulent processes, which will also act on the escaped high-energy electrons. Finally, a hard electron distribution appears in the sheath and subsequently produces synchrotron and SSC emissions, the latter could show a hard spectral shape, such that the hard-TeV spectrum occurs. Here, another point being emphasized is that the sheath is more beamed than the spine, e.g., the viewing angle of the sheath is small relative to the spine, this ensures high-energy  $\gamma$ -ray emission from the sheath to be more beamed. In fact, such explanation on the origin of the hard-TeV spectrum in Hard-TeV BL Lacs has been proposed to explain the TeV emissions from radio galaxy M87, where the layer is responsible for the TeV photons, while the debeamed spine accounts for the emissions from radio to GeV energies (Tavecchio & Ghisellini 2008). It is noted that such an idea is also used to clarify the origin of the high-energy particles generating during 2013 December 20  $\gamma$ -ray flare from 3C 279, a typical FSRQ (Lewis et al. 2019).

Up to now, an immediate question is that why the hard-TeV spectra only present in Hard-TeV BL Lacs and not in other typical HBLs, such as Mrk 421 and Mrk 501. The main reason could be the magnetic field in the jet. Actually, as shown in Table 1, we can see that the magnetic field strength,  $B'_0$ , of Mrk 421 and Mrk 501 are far larger than that of the Hard-TeV BL Lacs. The numerical simulations have shown that the development of sheath flow around a relativistic jet spine will help to clarify the partial stabilization of the jets, meanwhile the stabilization of spine and sheath as well as the velocity discrepancy of both will mainly depend on the magnetization (Hardee & Hughes 2003; Mizuno et al. 2007). In other words, as the magnetic field increases, the jet will become homogeneous,

both spine and sheath tend to have the nearly same velocity and properties, the spine-sheath structure will disappear. The conditions for generating the hard electron spectrum cannot be achieved, and the hard-TeV spectrum will be hardly produced.

## 5. Conclusion

Because the observation at energies above 580 GeV from 1ES 0229+200 (Aharonian et al. 2007a), the origin of the hard-TeV spectrum has been attracted more attentions, many attempts are made to explore the nature of the underlying particle acceleration mechanisms both theoretically and observationally. Up to 2018, the number of the Hard-TeV BL Lacs increases up to six, it is noted that the sample has been further enriched by recent observations (Acciari et al. 2020; Biteau et al. 2020), this thus makes this class of sources be emerging subclass of BL Lacs, where a prior efficient acceleration of the particle and an accompanying inefficient cooling must be matched each other. In this paper, we propose a leptonic one-zone model with a truncated conical structure to explore the origin of the hard-TeV spectra of six Hard-TeV BL Lacs, in which the electron population is injected at the base of the emitting region. During the evolution of the electrons along the jet, we merely consider the synchrotron radiative loss self-consistently. For comparison with six Hard-TeV BL Lacs, the model is also applied to two typical HBLs, Mrk 421 and Mrk 501. Our main results are summarized as follows:

(1) By fixing a broader electron energy distribution with the Lorentz factor from 1.0 to  $5.0 \times 10^5$ , our model can well reproduce the broadband SEDs of six Hard-TeV BL Lacs and two HBLs. Compared with two HBLs, the Hard-TeV BL Lacs require the higher cutoff energies to the electron distributions, at the order of  $10^6$ , larger than that of two HBLs by nearly one order of magnitude.

(2) Our SED modelings show that four Hard-TeV BL Lacs, 1ES 0229+200, 1ES 0347–121, RGB J0710+591 and 1ES 1101–232, have hard spectral index of 1.63, 1.75, 1.7 and 1.8, respectively, while 1ES 0414+009 and 1ES 1218+304 have softer spectral index of 2.1. On the other hand, in terms of SSC peak, five out of six have SSC peaks well above 1 TeV.

(3) The SED modelings to Hard-TeV BL Lacs require a lower magnetic field, at the order of mG, thus the jets are matter-dominated. While for Mrk 421 and Mrk 501, the required magnetic field are 1.0 G and 0.44 G, respectively. For Mrk 421, the relatively high magnetic field makes that the matter and the magnetic field energies are in equipartition. In contrast, the SED modelings of Mrk 501 and six Hard-TeV BL Lacs require the magnetic energy densities to be well below equipartition.

(4) As far as the jet power is concerned, only 1ES 1218+304 has large jet power more than the Eddington luminosity by a factor of 4.9, the other sources have a lower ratio of Eddington luminosity.

## Acknowledgments

We acknowledge the anonymous referee for insightful comments and valuable suggestions that have helped us improve the presentation. We also sincerely thank Dr. Luigi Costamante and David Paneque for sending us the multi-wavelength data sets. We acknowledge the financial supports from the growth project of young scientific and technological talents in colleges and universities in Guizhou Province (Qianjiaohao -KY-Zi[2020]221), and Scientific Research Foundation for Doctoral Program of Xingyi Normal University for Nationalities (20XYBS16).

## References

- Abdo, A. A., Ackermann, M., Agudo, I., et al. 2010b, *ApJ*, 716, 30  
 Abdo, A. A., Ackermann, M., Ajello, M., et al. 2010b, *ApJ*, 722, 520  
 Abdo, A. A., Ackermann, M., Ajello, M., et al. 2011a, *ApJ*, 736, 131  
 Abdo, A. A., Ackermann, M., Ajello, M., et al. 2011b, *ApJ*, 727, 129  
 Acciari, V. A., Aliu, E., Arlen, T., et al. 2009, *ApJ*, 695, 1370  
 Acciari, V. A., Aliu, E., Arlen, T., et al. 2010a, *ApJL*, 715, L49  
 Acciari, V. A., Aliu, E., Beilicke, M., et al. 2010b, *ApJL*, 709, L163  
 Acciari, V. A., Ansoldi, S., Antonelli, L. A., et al. 2020, *ApJS*, 247, 16  
 Acciari, V. A., Arlen, T., Aune, T., et al. 2011, *ApJ*, 729, 2  
 Aharonian, F., Akhperjanian, A. G., Barres de Almeida, U., et al. 2007a, *A&A*, 475, L9  
 Aharonian, F., Akhperjanian, A. G., Barres de Almeida, U., et al. 2007b, *A&A*, 473, L25  
 Aharonian, F., Akhperjanian, A. G., Bazer-Bachi, A. R., et al. 2007c, *A&A*, 470, 475  
 Aharonian, F. A., Khangulyan, D., & Costamante, L. 2008, *MNRAS*, 387, L206  
 Ahnen, M. L., Ansoldi, S., Antonelli, L. A., et al. 2018, *A&A*, 620, A181  
 Albert, J., Aliu, E., Anderhub, H., et al. 2007a, *ApJ*, 663, 125  
 Albert, J., Aliu, E., Anderhub, H., et al. 2007b, *ApJ*, 669, 862  
 Aliu, E., Archambault, S., Arlen, T., et al. 2014, *ApJ*, 782, 13  
 Asada, K., & Nakamura, M. 2012, *ApJL*, 745, L28  
 Asano, K., Takahara, F., Kusunose, M., et al. 2014, *ApJ*, 780, 64  
 Attridge, J. M., Roberts, D. H., & Wardle, J. F. C. 1999, *ApJL*, 518, L87  
 Baring, M. G., Böttcher, M., & Summerlin, E. J. 2017, *MNRAS*, 464, 4875  
 Biteau, J., Prandini, E., Costamante, L., et al. 2020, *NatAs*, 4, 124  
 Blumenthal, G. R., & Gould, R. J. 1970, *RvMP*, 42, 237  
 Böttcher, M., Dermer, C. D., & Finke, J. D. 2008, *ApJL*, 679, L9  
 Cao, G., & Wang, J. 2013, *PASJ*, 65, 109  
 Cao, G., & Wang, J. 2014, *ApJ*, 783, 108  
 Cerruti, M., Zech, A., Boisson, C., et al. 2015, *MNRAS*, 448, 910  
 Chen, L. 2017, *ApJ*, 842, 129  
 Cohen, M. H., Meier, D. L., Arshakian, T. G., et al. 2014, *ApJ*, 787, 151  
 Colomo, G., Mohamed, M., Wagner, S., et al. 2015, in 34th ICRC (ICRC2015), 34, The Hague, the Netherlands, 762  
 Costamante, L., Bonoli, G., Tavecchio, F., et al. 2018, *MNRAS*, 477, 4257  
 Costamante, L., Ghisellini, G., Giommi, P., et al. 2001, *A&A*, 371, 512  
 Şentürk, G. D., Errando, M., Böttcher, M., et al. 2013, *ApJ*, 764, 119  
 Dermer, C. D., Finke, J. D., Krug, H., et al. 2009, *ApJ*, 692, 32  
 Essey, W., Kalashev, O., Kusenko, A., et al. 2011, *ApJ*, 731, 51  
 Essey, W., & Kusenko, A. 2010, *Aph*, 33, 81  
 Falomo, R., Carangelo, N., & Treves, A. 2003, *MNRAS*, 343, 505  
 Fan, Z., Liu, S., & Fryer, C. L. 2010, *MNRAS*, 406, 1337  
 Finke, J. D., Dermer, C. D., & Böttcher, M. 2008, *ApJ*, 686, 181  
 Foffano, L., Prandini, E., Franceschini, A., et al. 2019, *MNRAS*, 486, 1741  
 Fossati, G., Maraschi, L., Celotti, A., et al. 1998, *MNRAS*, 299, 433  
 Franceschini, A., Rodighiero, G., & Vaccari, M. 2008, *A&A*, 487, 837  
 Ghisellini, G. 1999, *Aph*, 11, 11  
 Ghisellini, G., Celotti, A., Fossati, G., et al. 1998, *MNRAS*, 301, 451  
 Ghisellini, G., Maraschi, L., & Tavecchio, F. 2009, *MNRAS*, 396, L105  
 Ghisellini, G., Maraschi, L., & Treves, A. 1985, *A&A*, 146, 204

- Ghisellini, G., Righi, C., Costamante, L., et al. 2017, *MNRAS*, 469, 255
- Ghisellini, G., Tavecchio, F., & Chiaberge, M. 2005, *A&A*, 432, 401
- Hada, K., Doi, A., Wajima, K., et al. 2018, *ApJ*, 860, 141
- Hardee, P. E., & Hughes, P. A. 2003, *ApJ*, 583, 116
- Hillas, A. M. 1984, *ARA&A*, 22, 425
- Homan, D. C., Kadler, M., Kellermann, K. I., et al. 2009, *ApJ*, 706, 1253
- Homan, D. C., Lister, M. L., Kovalev, Y. Y., et al. 2015, *ApJ*, 798, 134
- Inoue, T., Asano, K., & Ioka, K. 2011, *ApJ*, 734, 77
- Jones, F. C. 1968, *PhRv*, 167, 1159
- Jorstad, S. G., Marscher, A. P., Morozova, D. A., et al. 2017, *ApJ*, 846, 98
- Kang, H. 2015, *JKAS*, 48, 9
- Katarzyński, K., Ghisellini, G., Mastichiadis, A., et al. 2006, *A&A*, 453, 47
- Kaufmann, S., Wagner, S. J., Tibolla, O., et al. 2011, *A&A*, 534, A130
- Kovalev, Y. Y., Lister, M. L., Homan, D. C., et al. 2007, *ApJL*, 668, L27
- Kravchenko, E. V., Kovalev, Y. Y., & Sokolovsky, K. V. 2017, *MNRAS*, 467, 83
- Lefa, E., Rieger, F. M., & Aharonian, F. 2011, *ApJ*, 740, 64
- Lei, M., Yang, C., Wang, J., et al. 2018, *PASJ*, 70, 45
- Lewis, T. R., Becker, P. A., & Finke, J. D. 2016, *ApJ*, 824, 108
- Lewis, T. R., Finke, J. D., & Becker, P. A. 2018, *ApJ*, 853, 6
- Lewis, T. R., Finke, J. D., & Becker, P. A. 2019, *ApJ*, 884, 116
- MacDonald, N. R., Jorstad, S. G., & Marscher, A. P. 2017, *ApJ*, 850, 87
- MacDonald, N. R., Marscher, A. P., Jorstad, S. G., et al. 2015, *ApJ*, 804, 111
- MAGIC Collaboration, Acciari, V. A., Ansoldi, S., et al. 2019, *MNRAS*, 490, 2284
- Mimica, P., & Aloy, M. A. 2012, *MNRAS*, 421, 2635
- Mizuno, Y., Hardee, P., & Nishikawa, K.-I. 2007, *ApJ*, 662, 835
- Moderski, R., Sikora, M., & Błażejowski, M. 2003, *A&A*, 406, 855
- Murase, K., Dermer, C. D., Takami, H., et al. 2012, *ApJ*, 749, 63
- Padovani, P. 2016, *A&ARv*, 24, 13
- Park, B. T., & Petrosian, V. 1996, *ApJS*, 103, 255
- Petrosian, V. 2012, *SSRv*, 173, 535
- Piner, B. G., Pant, N., & Edwards, P. G. 2010, *ApJ*, 723, 1150
- Piner, B. G., Pant, N., Edwards, P. G., et al. 2009, *ApJL*, 690, L31
- Potter, W. J., & Cotter, G. 2012, *MNRAS*, 423, 756
- Potter, W. J., & Cotter, G. 2013, *MNRAS*, 429, 1189
- Prosekin, A., Essey, W., Kusenko, A., et al. 2012, *ApJ*, 757, 183
- Rieger, F. M., Bosch-Ramon, V., & Duffy, P. 2007, *Ap&SS*, 309, 119
- Rueda-Becerril, J. M., Mimica, P., Aloy, M. A., et al. 2013, *EPJConf*, 61, 02007
- Rueda-Becerril, J. M., Mimica, P., & Aloy, M. A. 2014, *MNRAS*, 438, 1856
- Sahu, S., López Fortín, C. E., & Nagataki, S. 2019, *ApJL*, 884, L17
- Saugé, L., & Henri, G. 2004, *ApJ*, 616, 136
- Sokolovsky, K. V., Kovalev, Y. Y., Pushkarev, A. B., et al. 2011, *A&A*, 532, A38
- Spada, M., Ghisellini, G., Lazzati, D., et al. 2001, *MNRAS*, 325, 1559
- Stawarz, L., & Petrosian, V. 2008, *ApJ*, 681, 1725
- Stickel, M., Padovani, P., Urry, C. M., et al. 1991, *ApJ*, 374, 431
- Stoeckle, J. T., Morris, S. L., Gioia, I. M., et al. 1991, *ApJS*, 76, 813
- Tavecchio, F., & Ghisellini, G. 2008, *MNRAS*, 385, L98x
- Tavecchio, F., Ghisellini, G., Ghirlanda, G., et al. 2009, *MNRAS*, 399, L59
- Tavecchio, F., Ghisellini, G., Ghirlanda, G., et al. 2010, *MNRAS*, 401, 1570
- Tavecchio, F., Ghisellini, G., & Guetta, D. 2014, *ApJL*, 793, L18
- Urry, C. M., & Padovani, P. 1995, *PASP*, 107, 803
- Uzdensky, D. A. 2018, *MNRAS*, 477, 2849
- Yan, D., Zeng, H., & Zhang, L. 2012, *MNRAS*, 424, 2173
- Yan, D., Zhang, L., Yuan, Q., et al. 2013, *ApJ*, 765, 122
- Zakamska, N. L., Begelman, M. C., & Blandford, R. D. 2008, *ApJ*, 679, 990
- Zdziarski, A. A., & Bottcher, M. 2015, *MNRAS*, 450, L21
- Zech, A., & Lemoine, M. 2021, *A&A*, 654, A96
- Zhang, J., Liang, E.-W., Zhang, S.-N., et al. 2012, *ApJ*, 752, 157
- Zhang, J., Zhang, S.-N., & Liang, E.-W. 2013, *ApJ*, 767, 8
- Zheng, Y. G., Long, G. B., Yang, C. Y., et al. 2018, *MNRAS*, 478, 3855
- Zheng, Y. G., & Yang, C. Y. 2016, *MNRAS*, 457, 3535